AGU PUBLICATIONS

JGR

Journal of Geophysical Research: Space Physics

RESEARCH ARTICLE
10.1002/2017JA023942

Key Points:
- Atmospheric scattering causes errors in ground-based thermospheric wind and temperature measurements
- A radiative transfer model is developed, and it compares favorably with apparent vertical wind data
- Errors can reach 400 m/s and 200 K during geomagnetic storms at midlatitudes

Correspondence to:
B. J. Harding,
bhardin2@illinois.edu

Citation:
Harding, B. J., J. J. Makela, J. Qin, D. J. Fisher, C. R. Martinis, J. Noto, and C. M. Wrasse (2017), Atmospheric scattering effects on ground-based measurements of thermospheric vertical wind, horizontal wind, and temperature, *J. Geophys. Res. Space Physics*, *122*, 7654–7669, doi:10.1002/2017JA023942.

Received 6 FEB 2017
Accepted 25 APR 2017
Accepted article online 28 APR 2017
Published online 17 JUL 2017

Atmospheric scattering effects on ground-based measurements of thermospheric vertical wind, horizontal wind, and temperature

Brian. J. Harding[1], Jonathan J. Makela[1], Jianqi Qin[1], Daniel J. Fisher[1], Carlos R. Martinis[2], John Noto[3], and Cristiano M. Wrasse[4]

[1]Department of Electrical and Computer Engineering, University of Illinois at Urbana-Champaign, Urbana, Illinois, USA, [2]Center for Space Physics, Boston University, Boston, Massachusetts, USA, [3]Computational Physics, Inc., Springfield, Virginia, USA, [4]Instituto Nacional de Pesquisas Espaciais, São José dos Campos, Brazil

Abstract Ground-based Fabry-Perot interferometers routinely observe large vertical winds in the thermosphere, sometimes reaching over 100 m/s. These observations, which use the Doppler shift of the 630.0 nm airglow emission to estimate the wind, have long been at odds with theory. We present a summary of 5 years of data from the North American Thermosphere-Ionosphere Observing Network, showing that large apparent vertical winds are a persistent feature at midlatitudes during geomagnetic storms. We develop a radiative transfer model which demonstrates that these measurements can be explained as an artifact of the scattering of light in the troposphere. In addition to the example from midlatitudes, we apply the model to low latitudes, where we show that the postsunset vertical winds routinely measured over Brazil are explained in part by atmospheric scattering. Measurements of the horizontal wind and temperature are also affected, with errors reaching 400 m/s and 200 K in the most extreme cases.

1. Introduction

Vertical winds observed in the thermosphere utilizing ground-based Fabry-Perot interferometers (FPIs) have been reported for many years. In the polar cap, vertical winds of a few tens of m/s are common, and large upwellings up to 150 m/s are occasionally observed [*Rees et al.*, 1984; *Smith and Hernandez*, 1995; *Guo and McEwen*, 2003; *Ronksley*, 2016]. Most studies reporting vertical winds in the thermosphere have been conducted in the auroral zone, where winds of up to 50 m/s are common [*Wardill and Jacka*, 1986; *Crickmore et al.*, 1991; *Crickmore*, 1993; *Conde and Dyson*, 1995; *Aruliah and Rees*, 1995; *Ishii et al.*, 1999, 2001; *Greet et al.*, 2002; *Anderson et al.*, 2012; *Ronksley*, 2016], but larger winds of 100 m/s or more have also been observed [*Rees et al.*, 1984; *Price et al.*, 1995; *Innis et al.*, 1996, 1997, 1999; *Anderson et al.*, 2011]. Generally, downward winds have been seen on the equatorward edge of the auroral oval, and upward winds have been seen on the poleward edge. At midlatitudes, quiet time vertical winds of 20–40 m/s have been reported [*Hernandez*, 1982; *Biondi*, 1984]. During geomagnetic storms, downward vertical winds of 50–150 m/s have also been seen [*Sipler et al.*, 1995]. At low and equatorial latitudes, the vertical winds that have been measured are commonly within measurement error but are sometimes significant, reaching 20 m/s or more [*Biondi and Sipler*, 1985; *Fisher et al.*, 2015].

Measurements using other techniques also suggest the existence of large vertical winds but are generally more conservative. *Rieger* [1974] used a series of barium releases from a sounding rocket to report the first direct thermospheric vertical wind measurements, finding that they were generally small (~15 m/s), but one data point in the auroral region reached 42 m/s. A more recent rocket experiment in the auroral region failed to find vertical winds larger than 20 m/s [*Wescott et al.*, 2006]. Although the measurements are sensitive to knowledge of spacecraft orientation and velocity, significant results have also emerged from space-based in situ spectrometers. Atmospheric Explorer-C measured vertical winds that were often only a few m/s, but waves with peak-to-peak amplitudes of up to 100 m/s were sometimes seen at middle and high latitudes [*Spencer et al.*, 1976]. Initial measurements from Dynamics Explorer-2 indicated small 10–20 m/s vertical winds at lower latitudes and larger winds in the auroral region, with one event reaching 175 m/s [*Spencer et al.*, 1982]. A statistical analysis by *Innis and Conde* [2002] revealed that vertical wind variability was less than

30 m/s for 99% of the midlatitude samples, while for polar cap samples taken during high *AE* index, the corresponding probability was 68%. At equatorial latitudes, *Raghavarao et al.* [1993] found examples of 10–40 m/s downwelling associated with the equatorial thermosphere anomaly. Reviews of thermospheric vertical wind measurements are given by *Smith* [1998] and *Larsen and Meriwether* [2012].

Despite extensive previous research efforts, these large vertical wind observations have been difficult to reconcile with theory. Although vertical winds are usually smaller than horizontal winds, they have a larger impact on the dynamics, chemistry, and electrodynamics of the ionosphere-thermosphere system because vertical gradients of composition, density, and temperature are larger than horizontal gradients, so even a small vertical wind causes large advective transport and adiabatic temperature changes. The vertical wind associated with the "breathing" of an atmosphere in hydrostatic balance subjected to diurnal heating (the so-called barometric component) is only about 1 m/s [*Smith*, 1998]. Localized heat sources and divergent horizontal flows can drive the divergent component of the vertical wind [*Smith*, 1998]. However, many studies have found that an unreasonable scale height is needed to explain the large measured vertical winds with this mechanism [e.g., *Anderson et al.*, 2011]. The most recent theoretical development has been to relax the assumption of hydrostatic balance, which has allowed modeling of much larger vertical winds, reaching 100 m/s [*Deng et al.*, 2008]. However, deviations from hydrostatic balance are short-lived and cannot explain the large winds lasting more than an hour reported in some studies. Recently, *Makela et al.* [2014] observed 100 m/s apparent downward winds sustained for several hours during the 2 October 2013 geomagnetic storm at midlatitudes. This downward wind was observed by six independent FPIs spanning 10° in latitude and longitude. *Makela et al.* [2014] concluded that these large apparent vertical winds must be an artifact of some type of contamination and hypothesized that the source of contamination is energetic precipitating oxygen ions.

The purpose of this study is to offer an alternative hypothesis: atmospheric scattering. The only previous study to investigate the effects of atmospheric scattering on wind measurements was by *Abreu et al.* [1983], who concluded that the apparent convergence of the horizontal wind near auroral arcs could be an artifact of scattering. We believe it is timely to revisit this idea for four reasons. First, the proliferation of FPI networks in recent years has led to the discovery of new phenomena, such as large apparent vertical winds, that may be explained by atmospheric scatter. Second, the literature seems to have largely forgotten or neglected this effect; it has not been mentioned in over 20 years [*Price et al.*, 1995]. Third, computing power has increased tremendously since 1983, allowing us to solve the full radiative transfer equations instead of the simplified equations used by *Abreu et al.* [1983], which neglect azimuthal source variation and only use two terms in the Legendre polynomial expansion of scattered light. It is these simplifications which we believe led *Abreu et al.* [1983] to minimize the importance of the effect on temperature estimates, a critical point that we describe in section 5. Fourth, due to the growth of networks such as the Aerosol Robotic Network (AERONET) [*Holben et al.*, 2001], we can now monitor the radiative characteristics of aerosols in the lower atmosphere, the primary contributor to atmospheric scatter.

2. The Hypothesis of Atmospheric Scattering

FPIs measure the thermospheric wind and temperature by observing the spectrum of the 630.0 nm nighttime airglow emission. This emission originates from the ^1D-^3P transition of atomic oxygen and occurs near 250 km altitude. The Doppler shift of this emission is a proxy for the bulk motion of oxygen atoms and thus the bulk motion of the thermosphere. For an FPI observing in the vertical direction, the Doppler shift of the emission represents the vertical wind around 250 km altitude. Although daytime FPI observations are in principle possible, we only discuss nighttime observations in this paper.

The hypothesis of atmospheric scattering is built on the fact that the atmosphere is not perfectly transparent at visible wavelengths. Although most of the photons emitted at 250 km reach the ground unimpeded, ~ 10% scatter off molecules and aerosols in the troposphere, though the exact amount varies with the aerosol content [*Bodhaine et al.*, 1999; *Holben et al.*, 2001]. This process is displayed in Figure 1, which shows storm time conditions at northern midlatitudes. The vertically directed FPI measures the spectrum of the 630.0 nm emission, shown in the inset. The measured spectrum has two components: the direct spectrum, originating from photons emitted inside the field of view at 250 km above the FPI, and the scattered spectrum, originating from photons incident from all directions that have undergone one or more scattering events. The direct spectrum has no Doppler shift since there is no actual vertical wind. However, the scattered spectrum can have a large Doppler shift under two conditions: (1) there is a bright airglow region outside the field of

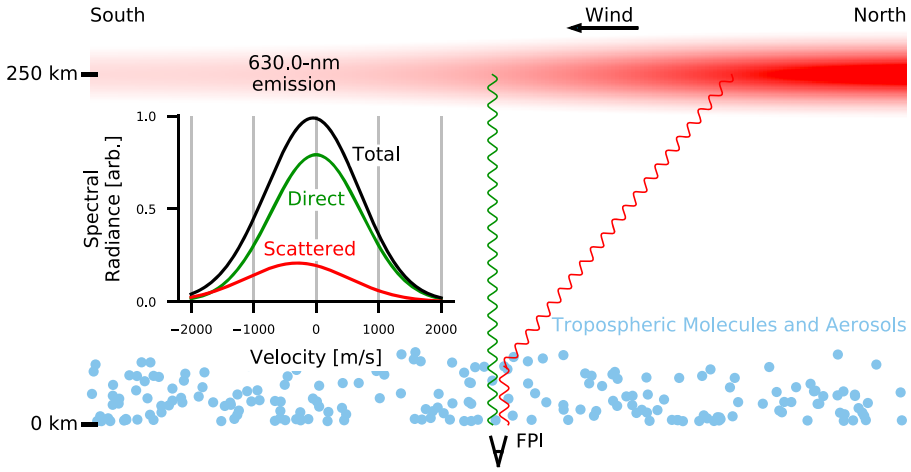

Figure 1. Scattering of airglow radiation in the lower atmosphere can cause an apparent vertical wind to be measured by a ground-based FPI during geomagnetic storms at midlatitudes (see text). Although only one ray is drawn, scattered light is incident from all directions. Not to scale. The inset displays the measured spectrum and its two components: direct and scattered light. Instead of wavelength, the *x* axis displays the equivalent Doppler velocity. The total measured spectrum has a Doppler shift which is falsely interpreted as a vertical wind.

view and (2) there is a large line-of-sight wind in the bright region. These two features commonly occur in the auroral region, near the edge of the equatorial ionization crests, and at dawn and dusk. They also occur during storms at midlatitudes: the airglow enhancement in the north is due to increased production of O (^1D) by energetic particle precipitation, and the southward wind is caused by the pressure gradient from auroral region heating. Although the scattered spectrum comprises photons incident from all directions, the majority of scattered photons originated in the north, where they were imbued with a blue shift by the horizontal wind. Thus, the total measured spectrum has a blue shift which is falsely interpreted as a downward vertical wind. As shown in the inset in Figure 1, even a small amount of scattering can cause an apparently large vertical wind (here −50 m/s). Although the previous explanation focused on narrow-field FPI measurements of the vertical wind, atmospheric scattering also affects wide-field FPIs and other interferometric instruments, and it causes errors in horizontal wind and temperature estimates, as we discuss in section 5. The airglow gradient is a key ingredient for apparent vertical winds. When airglow is uniform (e.g., during quiet times far from the auroral region), Doppler shifts from different directions cancel out in the zenith measurement, though temperature can be affected, as can horizontal wind measurements.

We begin in section 3 by presenting data from the North American Thermosphere-Ionosphere Observing Network (NATION), which shows that large apparent downward winds are a common midlatitude feature observed by multiple FPIs during multiple storms. In section 4, we describe our radiative transfer model, which uses data from an all-sky imager and AERONET to quantify the effect of atmospheric scatter on FPI measurements. We apply this model in section 5 to the storm observed by *Makela et al.* [2014]. The favorable comparison between the model output and the FPI data strongly suggests that atmospheric scattering fully explains the apparent vertical winds seen at midlatitudes during storms. Moving to equatorial latitudes, in section 6 we present a statistical study of vertical winds measured over Brazil, finding that they can be explained in part by atmospheric scatter.

3. NATION Vertical Winds: 2011–2016

In this section, we present data from NATION, a network which comprises five ground-based FPIs located across the eastern half of the United States, spanning 35.2°–42.3°N geographic latitude and 271.8°–279.6°E geographic longitude, with elevations below 1000 m. These data show that apparent vertical winds are routinely observed during storms at midlatitudes by multiple FPIs, suggesting that this feature cannot be explained as an instrumental artifact. Details of the network and instrumentation are described by *Makela et al.* [2014]. Data reduction and analysis algorithms are described by *Harding et al.* [2014] with the exception of how the Doppler reference is handled. Due to the lack of a suitable lab source of the 630.0 nm emission, FPIs are unable to measure absolute wavelengths, only relative wavelength shifts. The Doppler reference,

the wavelength corresponding to zero wind, is usually established by averaging a night of zenith observations, under the assumption that the average vertical wind is zero. For the events in this paper, the average vertical wind is not zero, so the Doppler reference is instead established by averaging the first five samples after sunset, under the assumption that the average vertical wind in the first hour of the night is zero. This would not be valid if the storm began before sunset, but that is not the case for any of the storms studied in this paper.

We present a superposed epoch analysis of NATION observations during 15 geomagnetic storms. These 15 storms were selected from all storms during the 5 year period from 1 September 2011 to 1 September 2016 which satisfy the following four criteria: (1) A decrease in the disturbance storm time (*Dst*) index of more than 50 nT in a 6 h window; (2) a *Dst* that drops to below −50 nT during the window; (3) the center of the window occurs between 0 and 7 UT; (4) and at least one of the five NATION instruments was operating and had excellent data quality (defined below). These criteria were chosen to ensure that only large storms are selected and that NATION is in a local time sector which allows observation of the entire main phase while in darkness.

Data quality is determined by a variety of factors. To pass the quality check, the FPI must have had no maintenance problems during the night (e.g., the laser calibration source was operating, and the CCD was cooling to at least −60°C). Samples with large uncertainty are excluded. Experience has shown that if the reported uncertainty is larger than 50 m/s, the sample is not trustworthy. Samples taken during extreme cloud cover are omitted. Most instruments are equipped with a cloud sensor, which measures the difference between the ambient temperature and the infrared sky temperature. When these two readings are within 10°C, cloud cover is dense enough to prevent any useful observations. To maximize the amount of data used in this analysis, we also include data from before cloud sensors were installed. One storm (14–15 July 2012) was manually removed because it was evident that clouds were present from the rapid variations in brightness measurements. All other storms during which cloud sensors were unavailable were included.

The final quality criterion is to omit low-brightness samples, as they are subject to contamination by hydroxyl emissions [*Hernandez*, 1974]. Although the hydroxyl line at 629.8 nm is usually an order of magnitude or more dimmer than the oxygen line at 630.0 nm, it can become important when the 630.0 nm line is dim, which occurs when the *F* region electron density is low or when the *F* region is lifted to high altitudes. *Ronksley* [2016] concludes that for their FPI in the polar cap, almost all of the vertical wind measurements larger than 50 m/s are attributable to hydroxyl contamination, and it is likely that some of the large vertical winds reported in the literature are as well. Unfortunately, it is difficult to generalize these results since the impact of the hydroxyl emission depends on details of the etalon design, optical filter, and analysis method. For the NATION FPI design, the hydroxyl emission causes an apparent blue shift in the emission (i.e., a negative apparent vertical wind for a zenith observation). For this analysis, we omit samples with a brightness below an instrument-specific threshold. This threshold is determined by analyzing all available quiet time vertical wind data, binning these data by brightness, and choosing the bin in which the average vertical wind is less than −5 m/s.

As long as 75% of the samples during a night pass the quality check, the night is included in the analysis (though the bad samples are excluded). Fifteen storms were identified, and an average of 1.9 instruments per storm passed the quality check. For each storm, we define the epoch time as the middle of the main phase and plot the vertical wind data relative to the epoch time. Specifically, the epoch time is defined as the midpoint between the time of most negative and most positive curvature in *Dst*, which correspond to storm sudden commencement and to the end of the main phase, where the end of the main phase has the additional requirement that it be a local minimum in *Dst*. Although cumbersome, this definition provides a better definition of the storm epoch time for the wide variety of storms used here, which include storms with multiple substorms and without a classical sudden commencement.

The results are shown in Figure 2. Figure 2 (top) shows the *Dst* index for all 15 storms relative to the epoch time. Figure 2 (bottom) compiles data from all FPIs available for each storm. The solid line is an average of the data in 30 min bins. From these data it is clear that there is a persistent downward wind seen during the main phase of storms at midlatitudes, between about −2 and +4 h since epoch. There are also apparent downward winds beginning about 7 h after the epoch time, which correspond to the storms that have a second drop in *Dst*. During these drops in *Dst*, the diffuse red aurora intensifies and moves equatorward, and strong equatorward winds develop in response to frictional and Joule heating in the auroral region. Both of

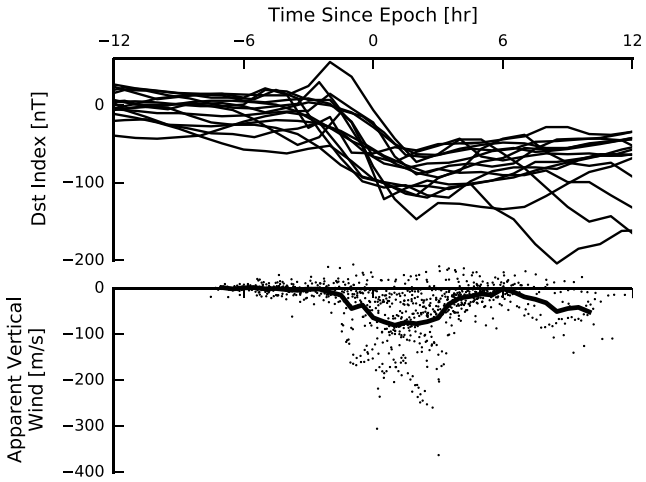

Figure 2. A superposed epoch analysis of 15 storms shows that apparent vertical winds are a common feature seen by FPIs at midlatitudes. The epoch time is defined as the midpoint between storm sudden commencement and the end of the main phase, as defined in the text. The disturbance storm time (*Dst*) index and NATION vertical wind measurements are plotted relative to the epoch time. The solid line is the average of the wind data in 30 min bins.

these are necessary conditions for atmospheric scattering to cause large apparent downward winds. Before the main phase, the measured vertical winds are near zero. During this time, the airglow intensity is uniform, and thus, the scattered Doppler shifts from different directions cancel.

Relative to the average behavior in Figure 2, there is a significant amount of variability. The primary contributor to this is storm-to-storm variability. The strength of the apparent vertical wind is controlled by the variability of the auroral intensity gradients and meridional winds. Individual inspection of each storm (not shown) indicates that large (less than −50 m/s) apparent downward winds were seen during all storms except one, 8–9 October 2013. This storm was relatively minor (*Dst* = −62 nT) and was the only one without a large equatorward wind during the main phase. The timing of the downward winds also contributes to the variability. While some vertical wind events last more than 6 h, some last only 2 h and occur at different epoch times. Another source of variability is that NATION spans 7° of latitude, and instruments at higher latitude observe stronger apparent vertical winds.

Despite the variability, the trend is clear: Apparent vertical winds are a common feature of the midlatitude thermosphere, observed across multiple instruments spanning several degrees of latitude and longitude. In the next section we describe the model which can offer quantitative support for the atmospheric scattering explanation.

4. Radiative Transfer Model

4.1. Radiative Transfer Equations

Radiative transfer theory provides the formalism to quantify the impact of atmospheric scatter on the transport of radiation through the atmosphere [*Hansen and Travis*, 1974; *Sobolev*, 1975]. Given an incident light source at the top of the atmosphere and the radiative properties of the atmosphere, the solution of the radiative transfer equations provides the intensity of the direct and scattered light at the ground. In our case, the spectral shape can be calculated by defining discrete wavelength bins and treating each bin as a separate radiative transfer problem, since Rayleigh and Mie scattering preserve wavelength. From *Hansen and Travis* [1974] and *Sobolev* [1975], the multiple-scattering equations to be solved are as follows (where we have included the missing $\frac{\omega}{4\pi}$ factor in equation (3.36) of *Hansen and Travis* [1974] and generalized the initial source term to J_0 instead of a specific point source such as the Sun):

$$u\frac{\mathrm{d}I(\tau,u,\phi)}{\mathrm{d}\tau} = -I(\tau,u,\phi) + J(\tau,u,\phi) \tag{1}$$

$$J(\tau,u,\phi) = \frac{\omega}{4\pi}\int_0^{2\pi}\int_{-1}^{1} P\left(u,u',\phi,\phi'\right) I\left(\tau,u',\phi'\right)\mathrm{d}u'\mathrm{d}\phi' + J_0(\tau,u,\phi) \tag{2}$$

The quantities to be solved are I, the specific intensity of scattered light, and J, the source function of scattered light. Each is a function of altitude and angle. The altitudinal variable is described in terms of optical depth, τ, which increases from 0 at the top of the atmosphere to τ_0, the optical thickness, at the ground. The angular variables are ϕ, the azimuth angle (degrees north of east), and u, the cosine of the zenith angle with respect to increasing τ, which varies from −1 (upward) to +1 (downward). The scattering phase function, $P(u, u', \phi, \phi')$, is the probability density function of a photon being scattered into direction (u, ϕ) given that a scattering event occurred and it was initially traveling in a direction (u', ϕ'). We assume elastic scattering, so we set ω, the single-scattering albedo, to 1. If we instead use $\omega = 0.75$ for the aerosol component (a lower bound based on AERONET measurements) and $\omega = 1$ for the molecular component, the vertical wind magnitude is reduced by about 9%. We ignore the effects of polarization and ozone absorption.

The use of these equations assumes that I and J do not vary significantly horizontally, which is a valid assumption in our case since most of the scattering occurs in the first few kilometers above the ground, where the mean free path of a photon is smaller than the horizontal scale size of variations in the scattered light field. For this same reason, we can neglect the curvature of the Earth in (1) and (2), although we must include it in the calculation of the initial source function, J_0.

There are two terms in (2), the first representing contributions from photons that have been scattered more than once and the second, J_0, representing photons incident from the airglow layer that are scattered for the first time. The airglow layer is approximated as a thin shell of emission at $h = 250$ km. It can be described by a function $f(x, y)$, the vertical column brightness of the emission, which varies horizontally. Our analysis does not depend upon absolute calibration, so $f(x, y)$ may be specified in arbitrary units. In this paper, we determine $f(x, y)$ by using data from an all-sky camera, discussed below in section 4.4.1. The model is not particularly sensitive to the choice of h; when it varies from 220 to 400 km, the resulting vertical wind varies by ∼7%. The model is sensitive mostly to the angular distribution of incoming light, which is measured directly by the camera and does not depend on h. Once we have specified $f(x, y)$, we can calculate J_0 as follows, noting that only downward directed rays (i.e., $u' > 0$) contribute to J_0 since the scattering region is illuminated only from above:

$$J_0(\tau, u, \phi) = \frac{\omega}{4\pi} \int_0^{2\pi} \int_0^1 P\left(u, u', \phi, \phi'\right) \sec\gamma' f(x', y') \exp\left(-\frac{\tau}{u'}\right) \mathrm{d}u' \mathrm{d}\phi' \tag{3}$$

where (x', y') is the point of origin of the light ray traveling in direction (u', ϕ') and γ' is the zenith angle of this ray at (x', y'). These quantities are calculated with spherical-Earth geometry, where $R_E = 6371$ km is the radius of the Earth:

$$\gamma' = \sin^{-1}\left(\frac{R_E}{R_E + h}\sqrt{1 - u'^2}\right) \tag{4}$$

$$\rho' = \left(R_E + h\right)\left(\cos^{-1} u' - \gamma'\right) \tag{5}$$

$$x' = -\rho' \cos\phi' \tag{6}$$

$$y' = -\rho' \sin\phi' \tag{7}$$

To solve (1) and (2), it is convenient to first write the formal solution to (1):

$$I(\tau, u, \phi) = \begin{cases} \displaystyle\int_0^{\tau} \frac{1}{u} J(\tau', u, \phi) \exp\left[\frac{-(\tau - \tau')}{u}\right] \mathrm{d}\tau' & \text{if } u > 0 \\ \displaystyle -\int_{\tau}^{\tau_0} \frac{1}{u} J(\tau', u, \phi) \exp\left[\frac{-(\tau - \tau')}{u}\right] \mathrm{d}\tau' & \text{if } u < 0 \end{cases} \tag{8}$$

4.2. Numerical Solution of Radiative Transfer Equations

We discretize the problem by defining M optical depths, N zenith angles, and R azimuth angles at which to evaluate I. In practice, we use $M = 10$, $N = 20$, and $R = 20$. The resolution of the model is given by

$$\Delta\tau = \frac{\tau_0}{M - 1} \qquad \Delta u = \frac{2}{N} \qquad \Delta\phi = \frac{2\pi}{R} \tag{9}$$

We define arrays **I** and **J** which contain the discretized versions of I and J:

$$\mathbf{I}_{m,n,r} = I\left(\tau_m, \quad u_n, \phi_r\right) \qquad \forall m \in [0, M-1], n \in [0, N-1], r \in [0, R-1] \tag{10}$$

$$\mathbf{J}_{m,n,r} = J\left(\tau_m + \Delta\tau/2, \quad u_n, \phi_r\right) \qquad \forall m \in [0, M-2], n \in [0, N-1], r \in [0, R-1] \tag{11}$$

Note that J is evaluated at the midpoints of the optical depth grid on which I is evaluated. The grid points are given by

$$\tau_m = m\Delta\tau \qquad u_n = (n + 0.5)\,\Delta u \qquad \phi_r = (r + 0.5)\,\Delta\phi \tag{12}$$

The solution to the coupled system of (8) and (2) is found numerically using the method of successive orders of scattering, described by *Hansen and Travis* [1974]. This method first computes the contribution from photons scattered once, then uses this information to compute the contribution from photons scattered twice, and so on. For small optical depths ($\tau \lesssim 1$), this method converges within several iterations. In this work, we iterate until the relative change in the solution is less than 10^{-4}. If we let the superscript k denote the iteration, then one iteration can be written as follows, where we have approximated the integrals in (8) and (2) as Riemann sums:

$$\mathbf{I}^k_{m,n,r} = \begin{cases} \displaystyle\sum_{m'=0}^{m-1} \frac{1}{u_n} \mathbf{J}^k_{m',n,r} \exp\left[-\frac{\Delta\tau}{u_n}\left(m - m' - \frac{1}{2}\right)\right]\Delta\tau & \text{if } u_n > 0 \\ \displaystyle -\sum_{m'=m}^{M-2} \frac{1}{u_n} \mathbf{J}^k_{m',n,r} \exp\left[-\frac{\Delta\tau}{u_n}\left(m - m' - \frac{1}{2}\right)\right]\Delta\tau & \text{if } u_n < 0 \end{cases} \tag{13}$$

$$\mathbf{J}^{k+1}_{m,n,r} = \frac{\omega}{4\pi} \sum_{r'=0}^{R-1} \sum_{n'=0}^{N-1} P(u_n, u_{n'}, \phi_r, \phi_{r'}) \left[\frac{\mathbf{I}^k_{m,n',r'} + \mathbf{I}^k_{m+1,n',r'}}{2}\right] \Delta u \Delta\phi \tag{14}$$

For the $k = 0$ iteration, the source function is simply the initial source function from (3):

$$\mathbf{J}^0_{m,n,r} = \frac{\omega}{4\pi} \sum_{r'=0}^{R-1} \sum_{n'=0}^{N-1} P(u_n, u_{n'}, \phi_r, \phi_{r'}) \sec\gamma' f(x', y') \exp\left(-\frac{\tau_m + \Delta\tau/2}{u_{n'}}\right) \Delta u \Delta\phi \tag{15}$$

where x', y', and γ' are calculated from $u_{n'}$ and $\phi_{r'}$ using (4)–(7). In practice, (13) and (14) can be computed with reduced resolution to improve runtime, while (15) must be computed at full resolution. This is because the airglow brightness, $f(x, y)$, typically has significant structuring, while the scattered light field is generally smooth.

After calculating the specific intensity of scattered light for each scattering order, $\mathbf{I}^k_{m,n,r}$, the total specific intensity of scattered light is the sum:

$$\mathbf{I}_{m,n,r} = \sum_{k=0}^{K-1} \mathbf{I}^k_{m,n,r} \tag{16}$$

where K is the total number of iterations.

4.3. Computation of Apparent Vertical Wind

Our goal is to use $\mathbf{I}_{m,n,r}$ to simulate the error in the wind estimated by an FPI. To do this requires two additional steps: including the wavelength dependence of the source and computing the spectrum observed by an FPI.

As mentioned above, the wavelength dependence is easy to incorporate. Since both molecular and aerosol scattering do not modify wavelength, there is no frequency redistribution, so each wavelength bin can be considered as a separate radiative transfer problem. We neglect the thermal motion of the scattering particles, as this is only important for molecular scattering, and the troposphere is much cooler than the thermosphere. We define $L = 20$ wavelength bins and run the model above with different $f(x, y)$ for each wavelength. All other quantities (e.g., optical thickness and scattering phase function) are the same, since the wavelength band of interest is only a few picometers. The spectrum of the emission at each location is modeled as a Gaussian, shifted by the line-of-sight wind and broadened by the temperature [see *Harding et al.*, 2014, (10)–(12)]. The line-of-sight wind is the dot product of the wind vector with the unit vector from the emission location at (x, y, h) to the FPI location at $(0, 0, 0)$. We assume that the actual vertical wind is zero everywhere and that the horizontal wind and temperature are uniform over the region contributing to the integral in (3),

a circle with a ~2000 km radius. The wind and temperature are inputs to our model, which can be taken from various sources, as discussed in section 4.4.3.

An ideal FPI would be sensitive to incoming light from only one direction, so to compute the flux observed by an ideal FPI, we would simply choose the grid point at $\tau = \tau_0$ (the ground) and at the angle corresponding to the direction the FPI is looking. However, real FPIs have finite fields of view, and more importantly, do not have perfect rejection of light from outside the field of view. The reflection of light off of the protective dome and entrance optics causes stray light to contaminate the measurement. To model this, we use an observation function which equals 1 inside the field of view (~2°) and decays to small values outside the field of view. It is assumed to be dependent only on the angle between the incident ray and boresight. This function, denoted $s(\theta)$, was measured carefully in the lab for one FPI from NATION, and it equals 10^{-3} at 10° and falls to a value of 10^{-5} at angles larger than 45°. Although these numbers are small, they cause a significant effect when integrated over the entire sky. The inclusion of stray light in the model causes the apparent vertical wind to increase by ~30–50%; thus, it is important to include even though its importance is secondary to atmospheric scatter. Although we only measured $s(\theta)$ for one FPI, we assume that it adequately characterizes $s(\theta)$ for the two different FPIs used in this work. This assumption is a nonnegligible source of uncertainty.

Based on the above discussion, the scattered flux, g_{sc}, measured by an FPI observing the scattered light with specific intensity $I(\tau, u, \phi)$ is modeled as

$$g_{sc} = \int_0^{2\pi} \int_{-1}^{1} s(\theta)\, I(\tau_0, u, \phi)\, du d\phi \tag{17}$$

where θ is defined as

$$\theta = \cos^{-1}\left(u u_0 + \sqrt{(1-u^2)(1-u_0^2)} \cos\left(\phi - \phi_0\right) \right) \tag{18}$$

and (u_0, ϕ_0) is the direction antiparallel to the boresight of the FPI. The integral is carried out numerically using the measured values of $s(\theta)$ and the calculated values of I from (16).

Until this point, we have only discussed the calculation of the flux of *scattered* light. We must also include the flux of direct, unscattered light, which is of course the dominant signal:

$$g_{dir} = \int_0^{2\pi} \int_{-1}^{1} s(\theta)\, \sec\gamma\, f(x,y)\, \exp\left(-\frac{\tau_0}{u}\right) du d\phi \tag{19}$$

where, as before, x, y, and γ are calculated from u and ϕ using (4)–(7). By sweeping over wavelength, we build the spectra of direct and scattered light observed by the FPI and add them to compute the total observed spectrum. An example is shown in the inset of Figure 1. Since the combination of the direct and scattered emission results in a line shape that is not exactly Gaussian, the wind and temperature error depend in principle on the analysis technique. FPIs do not measure the line shape directly; rather, they measure a fringe pattern which is the convolution of the line shape with the instrument function. To analyze real data, we use the technique described in *Harding et al.* [2014] to fit the convolution of a modified Airy function and a Gaussian. In the model described here, we exclude the instrument function in both the forward modeling and the estimation, fitting a Gaussian directly to the modeled line shape to determine the modeled apparent line-of-sight wind and apparent temperature. The apparent vertical wind is modeled by using a vertically directed boresight (i.e., $u_0 = 1$).

4.4. Inputs

In this section we describe the inputs to our radiative transfer model, which are the horizontal variation of airglow brightness, $f(x, y)$, the vertical optical thickness, τ_0, the scattering phase function, P, and the horizontal wind and temperature.

4.4.1. Brightness, $f(x, y)$

One of the main purposes of this study is to demonstrate that apparent vertical winds can result from atmospheric scattering if there is a relatively bright region outside the field of view. To accomplish this, we first need to determine the distribution of brightness, $f(x, y)$, for which we utilize data from an all-sky imager. An ideal all-sky imager is simply a camera observing the total brightness of the emission across the sky. Practical all-sky cameras have many calibration challenges, which are often specific to each instrument. Uncertainties with this calibration are significant and are the largest source of uncertainty with the model results in

this work. Since we use two different all-sky cameras in the case studies in sections 5 and 6, we will discuss their calibration issues separately.

For now, we will assume that the all-sky camera is able to provide the measured intensity at the ground for all ϕ and for all $u > 0$, denoted $I_{\text{meas}}(u, \phi)$. Computing $f(x, y)$ from this is complicated by the fact that $I_{\text{meas}}(u, \phi)$ is a combination of scattered light and direct light:

$$I_{\text{meas}}(u, \phi) = I(\tau_0, u, \phi) + \sec\gamma\, f(x, y)\, \exp\left(-\frac{\tau_0}{u}\right) \tag{20}$$

This equation cannot be solved directly for $f(x, y)$ since $I(\tau_0, u, \phi)$ depends on $f(x, y)$. Instead, we use an iterative approach:

$$f^{k+1}(x, y) = \frac{I_{\text{meas}}(u, \phi) - I^k(\tau_0, u, \phi)}{\sec\gamma\, \exp\left(-\frac{\tau_0}{u}\right)} \tag{21}$$

where the scattered light contribution at iteration k, $I^k(\tau, u, \phi)$, is computed from the source brightness estimate at iteration k, $f^k(x, y)$, using the model described above in section 4.2. To initialize, we set $I^0(\tau_0, u, \phi) = 0$, and we iterate five times, at which point the relative change in the solution is less than 10^{-4}. We note that in addition to correcting for the effects of scattered light, this process simultaneously corrects for extinction (via the exponential term) and the so-called van Rhijn effect (via the $\sec\gamma$ term).

In practice, the usable field of view of all-sky cameras does not reach down to the horizon, usually due to trees or buildings. For these missing values in $f(x, y)$, we use a zero-order hold extrapolation, filling them in with the nearest usable value. This extrapolation is a source of uncertainty in the model. Finally, we note that absolute calibration of the all-sky data is not necessary, so $I_{\text{meas}}(u, \phi)$ can be provided in arbitrary units.

4.4.2. Optical Thickness, τ_0, and Scattering Phase Function, P

The radiative characteristics of tropospheric aerosols are variable in space and time. To specify the aerosol contribution to τ_0 and P, which we denote as τ_0^{aero} and P^{aero}, we use measurements from AERONET [*Holben et al.*, 2001], which estimates them for multiple wavelengths at hundreds of locations around the Earth during daytime. For the midlatitude case study in section 5, we use data from the Billerica and Harvard_Forest AERONET sites, which are the two closest sites to Millstone Hill (~20 and 60 km, respectively). For each site, we interpolate to 630.0 nm and average the presunset and postsunrise values. Averaging between the two sites, we get $\tau_0^{\text{aero}} = 0.067$ for the night in question. The result is not sensitive to minor changes in P, so we simply use the estimated P^{aero} at 21 UT on 2 October 2013 at 670 nm.

For the equatorial case, the nearest AERONET site (Petrolina_SONDA) is 500 km away from the FPI measurement location (Cariri, Brazil). This adds considerable uncertainty to the result. For simplicity, we use $\tau_0^{\text{aero}} = 0.1$, which is a typical value for September–March, though it is usually smaller for March–September. A more complex seasonally dependent analysis was performed, and although the results changed quantitatively, they did not change qualitatively, and the same conclusions were reached. For example, if $\tau_0^{\text{aero}} = 0.05$ is used instead, the slope in Figure 6 is reduced, but the positive correlation remains. We use the same P^{aero} as above.

In addition to the Mie scattering contribution from aerosols, there is also a Rayleigh scattering contribution from N_2 and O_2 molecules, which is not negligible. The radiative characteristics of molecular scattering are

$$P^{\text{mol}}(\theta) = \frac{3}{4}\left(1 + \cos^2\theta\right) \tag{22}$$

$$\tau_0^{\text{mol}} = 0.0558 \tag{23}$$

where τ_0^{mol} is taken from *Bodhaine et al.* [1999]. The total τ_0 and P are

$$\tau_0 = \tau_0^{\text{aero}} + \tau_0^{\text{mol}} \tag{24}$$

$$P(\theta) = \frac{\tau_0^{\text{aero}} P^{\text{aero}}(\theta) + \tau_0^{\text{mol}} P^{\text{mol}}(\theta)}{\tau_0} \tag{25}$$

Using this weighted average assumes that the altitude profiles of the aerosol and molecular extinction coefficients are similar, which is a reasonable approximation because both have exponential profiles (though the scale heights are different), and most of the scattering occurs in the first few kilometers above the ground. Note that P is specified here as a function of the scalar scattering angle, θ, while in (14) and (15) it is given as a function of incident angle (u, ϕ) and scattered angle (u', ϕ'). The connection is given by (18). The optical

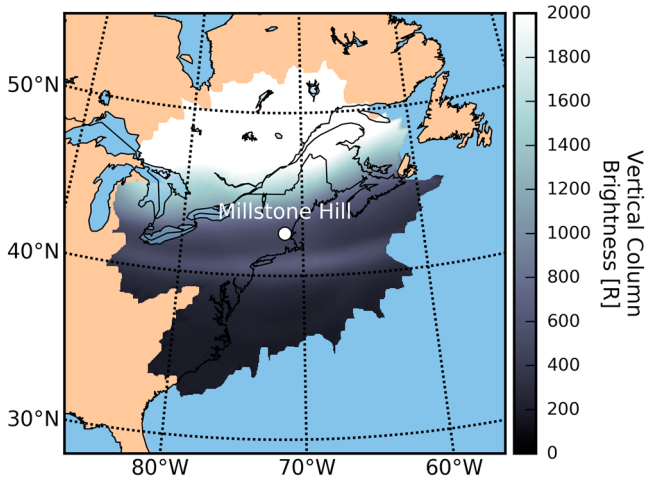

Figure 3. The airglow source function $f(x, y)$, shown as a function of latitude and longitude at 05:06 UT on 2 October 2013. The diffuse red aurora is seen in the north, and a subauroral red (SAR) arc is seen at 40°N. The irregular outline is due to trees obstructing the field of view.

thickness we use is smaller than the value used by *Abreu et al.* [1983] ($\tau_0 = 0.27$), and our scattering phase function is more forward peaked.

4.4.3. Horizontal Wind and Temperature

The final inputs are the wind and temperature, which determine the line shape of the airglow source emission. The only available data for these are the FPI measurements, which is problematic since we are modeling the error in these quantities. We use two different approaches for the midlatitude and equatorial cases.

When the FPI is observing a bright region of the sky, the ratio of direct to scattered light is large, and the error in the wind and temperature estimates is small. At midlatitudes during storms, the brightest region is poleward (i.e., north). Thus, the meridional wind can be determined directly from the line-of-sight wind measured to the north, assuming there is no actual vertical wind. The temperature can also be accurately determined this way. It is impossible to measure an accurate zonal wind, but since the airglow intensity gradient is purely meridional, our model is not sensitive to the value of the zonal wind, so we set it to zero.

For the equatorial case, the airglow intensity gradient is not purely zonal or meridional, and it varies significantly from season to season and night to night. Furthermore, the brightest regions of the sky are often at higher zenith angles than those observed by the FPI (45°), so all observations are affected by scatter. For these reasons, we rely on a climatological model of the winds, the Horizontal Wind Model 2014 [*Drob et al.*, 2015]. This model cannot be used for the midlatitude analysis, because it does not capture storm time dynamics. For temperature, we use the NRLMSISE-00 model [*Picone et al.*, 2002], though our results are not significantly sensitive to temperature.

5. Midlatitude Stormtime Case Study

In this section we apply the model in section 4 to the storm of 1–2 October 2013 described by *Makela et al.* [2014], when large apparent vertical winds were observed across the Eastern United States by the FPIs composing NATION and the FPI at the Millstone Hill Observatory. For this study, we use data from the FPI at Millstone Hill (latitude 42.6°, longitude −71.5°, elevation 130 m), which has a colocated all-sky camera operated by the Boston University Imaging Group.

The all-sky camera takes data at a 400 s cadence. Calibration of the raw data is described in the appendix section of *Baumgardner et al.* [2008], and it accounts for the effects of vignetting, spectral background, and flat fielding. In this work, we include an additional calibration step to account for the effect of stray light. As with the FPI, the all-sky camera is affected by stray light: photons from bright regions of the sky can scatter off of the dome or elsewhere in the optical path and be registered as an artificial increase in flux from darker regions of the sky. To correct for this, we assume that stray light causes a uniform additional flux across the raw image. The regions of the image outside of the field of view are illuminated solely by stray light and are used to determine the stray light contribution, which is subtracted from the entire image. This process adds

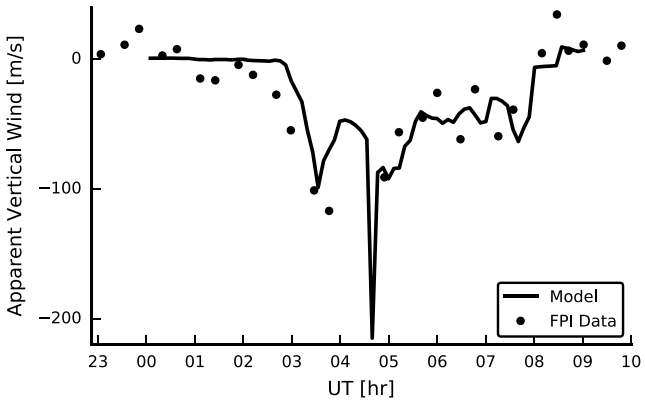

Figure 4. The Millstone Hill FPI and all-sky camera are used to compare the measured and modeled apparent vertical winds during the geomagnetic storm of 1–2 October 2013. Statistical error in the FPI data is 1–2 m/s.

a considerable amount of uncertainty, since we expect that stray light is not uniform and instead contains a significant specular component. Adequately characterizing the stray light susceptibility in the lab is difficult, and correcting for it is more difficult still. We believe that the procedure used here, though not perfect, is a valid first approximation. The inclusion of this stray light correction increases the modeled apparent vertical wind by 30–80%. An example $f(x, y)$ is shown in Figure 3.

For each all-sky image, we determine $f(x, y)$ and use our radiative transfer model to compute the apparent vertical wind. As mentioned above, the model input values for temperature and meridional wind are set to the estimates from the northward looking FPI observation, since it is minimally affected by scatter. The zonal wind is set to zero. We compare the model output with data from the FPI at Millstone Hill, which is described by *Makela et al.* [2014]. This FPI has a field of view of 1.8°, and its data have a negligible statistical uncertainty of 1–2 m/s. The comparison is shown in Figure 4. Before 02:30 UT, the measured and modeled apparent vertical winds are nearly zero. Around 02:30–03:00 UT, a decrease in the measured wind is followed shortly by a decrease in the modeled wind. Between 03:00 and 08:00 UT, the modeled vertical wind fluctuates between −100 and −50 m/s, roughly matching the measurement. One striking exception is at 04:45 UT, when a large downward pulse is seen in the modeled wind. The duration of this pulse is short, lasting only a single all-sky image. Unfortunately, no data are available from the FPI between 04:00 and 05:00 UT, as it was taking a series of flat field images. However, *Makela et al.* [2014] report a similar pulse seen in all five NATION FPIs at this time. At 08:00 UT, both the measured and modeled winds return to near-zero values. The correspondence between the model and the data strongly suggests that the large apparent vertical winds seen by midlatitude FPIs during storms is fully explained by atmospheric scatter.

In addition to errors in vertical wind measurements, atmospheric scatter causes errors in horizontal wind and temperature measurements. We ran the same model described above, except that we changed the pointing direction of the FPI to the south at a zenith angle of 45°. This measurement, which is used to determine the meridional wind, is significantly affected by atmospheric scatter because it is observing a dark region of the sky. The results are compared with the model input values for meridional wind and temperature, and the error is shown in Figure 5. During 03:00–08:00 UT, the line-of-sight wind is in error by 100–400 m/s in a direction toward the FPI. Combined with the north looking measurement (which is looking at the bright aurora and is minimally contaminated), this error manifests as an apparent convergence in the horizontal wind field. This likely explains the horizontal convergence that is commonly reported at midlatitudes during storms [e.g., *Hernandez and Roble*, 1976; *Hernandez et al.*, 1982; *Biondi*, 1984; *Makela et al.*, 2014] and perhaps explains some convergences reported near the aurora [e.g., *Anderson et al.*, 2011]. Of course, there are many other effects which can cause apparent convergences, such as inaccurate Doppler referencing, hydroxyl contamination, instrumental or laser calibration fluctuations, and actual vertical winds that are not properly handled in the analysis.

The model indicates that the temperature measured to the south is artificially high by 75–200 K during 03:00–08:00 UT, also shown in Figure 5. This causes an apparent temperature increase from the north, where it is measured accurately, to the south, a distance of about 500 km. This result is in stark contrast with *Abreu et al.* [1983], who claim that temperature measurements are unaffected by scatter. Unfortunately, this

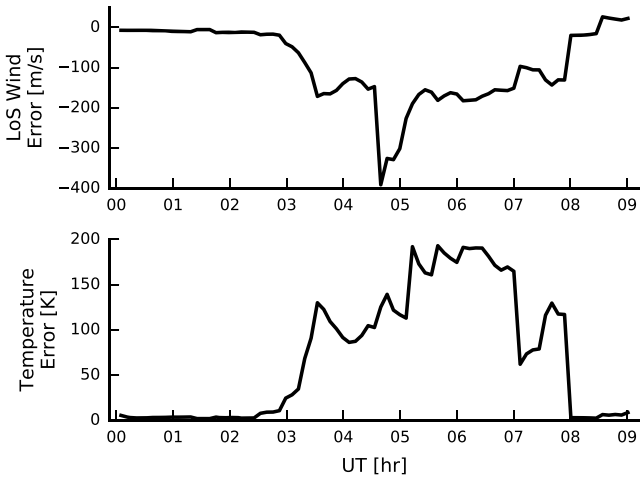

Figure 5. The Millstone Hill all-sky camera is used to model the error in the line-of-sight (LOS) wind and temperature measured by an FPI looking to the south at a 45° zenith angle during the geomagnetic storm of 1–2 October 2013. LOS wind is defined as positive away from the FPI.

erroneous claim has been used to downplay the effects of scatter in the literature [e.g., *Hernandez et al.*, 1982; *Sica*, 1984; *Price et al.*, 1995]. A common argument is that since the temperatures measured to the south and to the north are different, then atmospheric scatter effects must not be important. Our work invalidates this argument and thus questions previous measurements of horizontal convergences, temperatures, and vertical winds in the midlatitude thermosphere. For some studies, the FPIs were stationed at high elevations, where atmospheric scatter is less effective (e.g., 2700 m for *Hernandez et al.* [1982]). However, we note that stray light alone can cause apparent vertical winds and convergences.

This result highlights the difficulty with interpreting FPI measurements, as the artifacts introduced by atmospheric scattering can seem physically self-consistent. After all, the bright airglow associated with the diffuse red aurora is a sign of auroral energy input, which would be expected to drive vertical winds. Downward vertical winds would be associated with converging horizontal winds and a temperature increase. Moreover, for instruments that are located farther from the aurora, these effects would be smaller. Unfortunately, as our model shows, all of these observations can also be explained as artifacts of atmospheric scattering.

6. Equatorial Statistical Study

In this section, we use our model to explain the climatological vertical winds reported by *Fisher et al.* [2015] at equatorial latitudes as artifacts of atmospheric scatter. After averaging 5 years of data from Cariri and Cajazeiras, Brazil, on a month-by-month basis, they see a 20 m/s postsunset downward wind near the December solstice. Near the March equinox, there is also a postsunset downward wind, but it is weaker, and followed an hour later by a 10 m/s upward wind. They also report a presunrise downward wind, but in this work we focus on the postsunset winds. Unlike in section 5, the airglow brightness gradient that leads to errors from atmospheric scatter does not arise from the aurora, but rather from the combination of the gradient at the solar terminator and the gradient at the edge of the equatorial ionization crest.

We use data taken in Cariri, Brazil (7.4°S, 36.5°W), which has a colocated FPI and all-sky camera. The FPI design is described by *Makela et al.* [2009], and, as above, we use the analysis algorithm described by *Harding et al.* [2014] to determine the measured vertical wind.

The all-sky camera belongs to the Brazilian National Institute for Space Research (INPE) and is operated by the Federal University of Campina Grande (UFCG). The airglow imager includes the appropriate lenses to form an all-sky telecentric image near the 3 inch diameter filter plane, and to reimage achromatically onto the CCD chip. The primary (front) lens in the 3 inch system is a 24 mm, f/4.0 medium-format achromatic fisheye lens, while the final lens in front of the CCD is an ultrafast f/0.95 Canon 50 mm objective. The OI 630.0 nm filter has a bandwidth of 2.0 nm and is mounted in the filter wheel. The CCD is equipped with a back-illuminated e2v CCD47-10 chip with 1024 × 1024 pixels, 13.3μm square pixels with a total area of 13.3 mm × 13.3 mm. In order to enhance the signal-to-noise ratio, the images were binned down to a resolution of 512 × 512

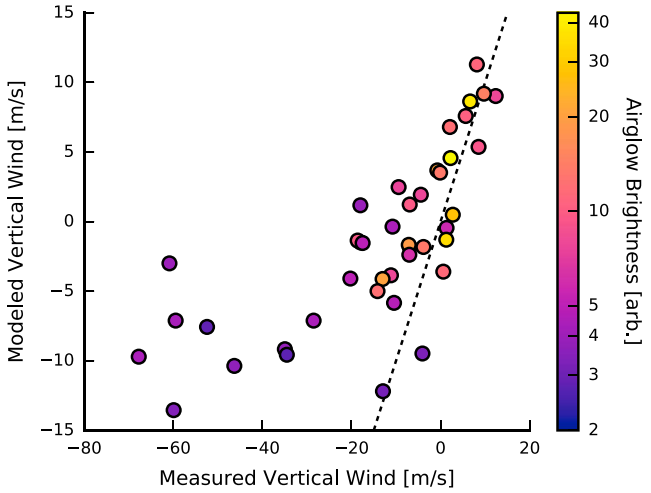

Figure 6. The Cariri FPI and all-sky camera are used to compare the measured and modeled apparent vertical winds for 21 nights during 2013–2015. The wind during the first hour and second hour are averaged to generate two data points per night. The dashed line has a slope of 1 and is a reference for perfect agreement between model and data. The color of each point represents the average brightness measured by the FPI during that hour.

pixels. The CCD has a high-quantum efficiency in the visible (greater than 95% at 630.0 nm) and NIR spectrum and a low dark current (4×10^{-4} electrons/pixel/s at −70°C). The CCD has a thermoelectric cooling system reaching temperatures around −70°C. We correct the raw data for stray light as described above. No flat-field calibration data are available, so we perform a rudimentary flat-field correction using the known solid angle of each pixel and projected aperture area. The uncertainty with this correction is significant, so the magnitude of the modeled apparent vertical wind should be treated with caution. However, the sign is trustworthy, as are relative variations in the magnitude from night to night. This is also true for the uncertainty associated with the optical thickness, as discussed in section 4.4.2.

For this analysis, we run the model for multiple nights selected from the 2013–2015 period, which has higher quality FPI data than the previous years. We included all nights meeting the following criteria: (1) both the FPI and all-sky camera were operating during the first 2 h after sunset with no maintenance problems; (2) no clouds were present in a visual inspection of the all-sky images; and (3) the moon was down during the first 2 h after sunset. These criteria were met by 21 nights. For each night, we run the model for every all-sky image taken during the first hour after sunset and average the resulting apparent vertical winds, comparing it to the average FPI measurement during this time, where the average is weighted by the FPI measurement uncertainties. We also perform this analysis for the second hour after sunset. Except for the wider FPI field of view (2.5°), and the aerosol optical thickness (0.1), the same parameters that were used in the previous section are used here. As mentioned in section 4.4.3, the model input value for the horizontal wind is taken from the Horizontal Wind Model 2014, and the temperature is taken from NRLMSISE-00.

The results are shown in Figure 6, which contains two points for every night: one each for the first and second hours. If the model and the data agreed perfectly, the results would lie along the dotted line, shown for reference. Each point is colored according to the airglow brightness, as measured by the FPI, averaged over the hour in question. The FPI is not absolutely calibrated, so we report the brightness in arbitrary units.

Except for several of the points taken during periods of low brightness, the agreement between the modeled and measured vertical winds is compelling. Even more compelling is the fact that the apparent winds have positive and negative values; any spectral contaminant or systematic error would be expected to yield purely negative or purely positive errors. The fact that both errors seem to be explained by our radiative transfer model is strong evidence that atmospheric scatter is a significant contributor to the vertical winds reported by *Fisher et al.* [2015].

The low-brightness outliers comprise vertical wind measurements that are quite large, reaching almost −70 m/s. The modeled vertical winds at these times are much smaller, but still negative. The difference could be due to the uncertainty in the calibration and optical thickness described above, but since all the outliers

have such low brightness, a more likely explanation is a spectral contaminant such as the hydroxyl emission. Independent validation of this explanation is the subject of current research.

7. Conclusion

Vertical winds in the thermosphere are commonly reported in the literature, and we have shown a superposed epoch analysis of NATION data which indicates a consistent and repeatable apparent downward wind across multiple instruments and multiple storms. We have developed a radiative transfer model which quantifies the effect of atmospheric scatter on FPI measurements. This model incorporates data from a colocated all-sky camera to determine the brightness of the red line emission across the sky, and it characterizes the effect of tropospheric aerosol and molecular scattering on the measured spectrum (and thus the wind and temperature estimates) at the ground. Application of this model to a case study of the 1–2 Oct 2013 storm at Millstone Hill shows good agreement between the measured vertical winds and the apparent, erroneous vertical winds caused by atmospheric scatter. At equatorial latitudes, a statistical study using 21 nights of post-sunset data found a positive correlation between measured vertical winds and modeled apparent vertical winds caused by scatter. In addition to FPIs, all ground-based optical instruments are affected by atmospheric scattering, including Michelson interferometers and all-sky cameras. This effect should also be considered for ground-based wind and temperature measurements using other emission lines. For example, the larger optical thickness of the atmosphere at the O (^1S) wavelength of 557.7 nm suggests larger scattering effects, but even for mesospheric infrared emissions such as the OH and the O_2 bands, gravity waves can cause large airglow gradients, which may create nonnegligible scattering effects.

As detector technology improves, we are beginning an era in which statistical errors in FPI measurements are becoming negligible compared to systematic errors such as atmospheric scatter, stray light, and hydroxyl contamination. An improved quantitative understanding of the thermospheric wind and temperature will require an improved quantitative understanding of these errors. In the case of atmospheric scatter, this requires the colocation of FPIs with all-sky cameras, improved characterization of the flat fields, responsivity, filter passbands, and stray light susceptibility of both FPIs and all-sky cameras, and a suitable quantification of the aerosol optical thickness. Coincident observations of vertical winds using different modalities would be an invaluable validation tool, as nonoptical or non-ground-based measurement modalities are not affected by atmospheric scatter.

In principle, correcting FPI data for the effects of atmospheric scatter is straightforward. We must simply compute the spectrum of scattered light and remove it from the FPI data. In practice, the uncertainties in the model inputs are significant. The most important uncertainties are modeling the stray light susceptibility of the FPI, removing stray light from the all-sky camera data, calibrating the all-sky camera, cross-calibrating FPI and all-sky radiances, and specifying the radiative properties of the atmosphere (i.e., aerosol optical thickness, scattering phase function, and single-scattering albedo). Quantifying these uncertainties is difficult, particularly for AERONET, which does not provide uncertainties, and for stray light, which is a challenging measurement. These factors yield modeled vertical wind uncertainties reaching 100% during periods of large apparent vertical winds, which prevents meaningful results. Future work will describe the development of correction algorithms.

Acknowledgments
The authors thank J. Baumgardner, J. Meriwether, and S. Solomon for useful discussions. We also recognize Stephen H. Jones, Brent N. Holben, and Enio B. Pereira for their efforts in establishing and maintaining the Billerica, Harvard_Forest, and Petrolina_SONDA AERONET sites. The Embrace/INPE Program from MCTI provided the Cariri all-sky data. The *Dst* index data were obtained from the World Data Center for Geomagnetism in Kyoto, Japan. The FPI data in this work are available on the Madrigal database or can be made available by request. This material is based upon work supported by the National Science Foundation under grant NSF AGS 14-52291, by the National Science Foundation Graduate Research Fellowship under grant DGE-1144245, and by NASA under grant NNX14AD46G. Any opinions, findings, and conclusions or recommendations expressed in this material are those of the author(s) and do not necessarily reflect the views of the National Science Foundation. This work was partially supported by the CNPq under the project 310926/2014-9.

References

Abreu, V., G. A. Schmitt, P. Hays, J. Meriwether, C. Tepley, and L. L. Cogger (1983), Atmospheric scattering effects on ground-based measurements of thermospheric winds, *Planet. Space Sci.*, *31*(3), 303–310, doi:10.1016/0032-0633(83)90080-6.

Anderson, C., T. Davies, M. G. Conde, P. Dyson, and M. J. Kosch (2011), Spatial sampling of the thermospheric vertical wind field at auroral latitudes, *J. Geophys. Res.*, *116*, A06320, doi:10.1029/2011JA016485.

Anderson, C., M. G. Conde, and M. G. McHarg (2012), Neutral thermospheric dynamics observed with two scanning Doppler imagers: 2. Vertical winds, *J. Geophys. Res.*, *117*, A03305, doi:10.1029/2011JA017157.

Aruliah, A. L., and D. Rees (1995), The trouble with thermospheric vertical winds: geomagnetic, seasonal and solar cycle dependence at high latitudes, *J. Atmos. Terr. Phys.*, *57*(6), 597–609, doi:10.1016/0021-9169(94)00100-3.

Baumgardner, J. L., J. Wroten, J. Semeter, J. Kozyra, M. Buonsanto, P. Erickson, and M. Mendillo (2008), A very bright SAR arc: Implications for extreme magnetosphere-ionosphere coupling, *Ann. Geophys.*, *25*(12), 2593–2608, doi:10.5194/angeo-25-2593-2007.

Biondi, M. A. (1984), Measured vertical motion and converging and diverging horizontal flow of the midlatitude thermosphere, *Geophys. Res. Lett.*, *11*(1), 84–87, doi:10.1029/GL011i001p00084.

Biondi, M. A., and D. P. Sipler (1985), Horizontal and vertical winds and temperatures in the equatorial thermosphere: Measurements from Natal, Brazil during August–September 1982, *Planet. Space Sci.*, *33*(7), 817–823, doi:10.1016/0032-0633(85)90035-2.

Bodhaine, B., N. Wood, E. Dutton, and J. Slusser (1999), On Rayleigh optical depth calculations, *J. Atmos. Oceanic Technol.*, *16*, 1854–1861, doi:10.1175/1520-0426(1999)016<1854:ORODC>2.0.CO;2.

Conde, M. G., and P. Dyson (1995), Thermospheric vertical winds above Mawson, Antarctica, *J. Atmos. Terr. Phys.*, *57*(6), 589–596, doi:10.1016/0021-9169(94)00099-A.

Crickmore, R. I. (1993), A comparison between vertical winds and divergence in the high-latitude thermosphere, *Ann. Geophys.*, *11*, 728–733.

Crickmore, R., J. Dudeney, and A. Rodger (1991), Vertical thermospheric winds at the equatorward edge of the auroral oval, *J. Atmos. Terr. Phys.*, *53*(6–7), 485–492, doi:10.1016/0021-9169(91)90076-J.

Deng, Y., A. D. Richmond, A. J. Ridley, and H.-L. Liu (2008), Assessment of the non-hydrostatic effect on the upper atmosphere using a general circulation model (GCM), *Geophys. Res. Lett.*, *35*, L01104, doi:10.1029/2007GL032182.

Drob, D. P., et al. (2015), An update to the Horizontal Wind Model (HWM): The quiet time thermosphere, *Earth Space Sci.*, *2*, 301–319, doi:10.1002/2014EA000089.

Fisher, D. J., J. J. Makela, J. W. Meriwether, R. A. Buriti, Z. Benkhaldoun, M. Kaab, and A. Lagheryeb (2015), Climatologies of nighttime thermospheric winds and temperatures from Fabry-Perot interferometer measurements: From solar minimum to solar maximum, *J. Geophys. Res. Space Physics*, *120*, 6679–6693, doi:10.1002/2015JA021170.

Greet, P. A., J. L. Innis, and P. L. Dyson (2002), Thermospheric vertical winds in the auroral oval/polar cap region, *Ann. Geophys.*, *20*(12), 1987–2001, doi:10.5194/angeo-20-1987-2002.

Guo, W., and D. McEwen (2003), Vertical winds in the central polar cap, *Geophys. Res. Lett.*, *30*(14), 1–4, doi:10.1029/2003GL017124.

Hansen, J. E., and L. D. Travis (1974), Light scattering in planetary atmospheres, *Space Sci. Rev.*, *16*(4), 527–610, doi:10.1007/BF00168069.

Harding, B. J., T. W. Gehrels, and J. J. Makela (2014), Nonlinear regression method for estimating neutral wind and temperature from Fabry-Perot interferometer data, *Appl. Opt.*, *53*(4), 666–673, doi:10.1364/AO.53.000666.

Hernandez, G. (1974), Contamination of the OI(3P2-1D2) emission line by the (9-3) band of OH X2II in high-resolution measurements of the night sky, *J. Geophys. Res.*, *79*(7), 1119–1123, doi:10.1029/JA079i007p01119.

Hernandez, G. (1982), Vertical motions of the neutral thermosphere at midlatitude, *Geophys. Res. Lett.*, *9*(5), 555–557, doi:10.1029/GL009i005p00555.

Hernandez, G., and R. G. Roble (1976), Direct measurements of nighttime thermospheric winds and temperatures: 2. Geomagnetic storms, *J. Geophys. Res.*, *81*(28), 5173–5181, doi:10.1029/JA081i028p05173.

Hernandez, G., R. G. Roble, E. C. Ridley, and J. H. Allen (1982), Thermospheric response observed over Fritz Peak, Colorado, during two large geomagnetic storms near Solar Cycle Maximum, *J. Geophys. Res.*, *87*(A11), 9181, doi:10.1029/JA087iA11p09181.

Holben, B. N., et al. (2001), An emerging ground-based aerosol climatology: Aerosol optical depth from AERONET, *J. Geophys. Res.*, *106*(D11), 12,067–12,097, doi:10.1029/2001JD900014.

Innis, J. L., and M. G. Conde (2002), High-latitude thermospheric vertical wind activity from Dynamics Explorer 2 Wind and Temperature Spectrometer observations: Indications of a source region for polar cap gravity waves, *J. Geophys. Res.*, *107*(A8), 1–17, doi:10.1029/2001JA009130.

Innis, J. L., P. Greet, and P. Dyson (1996), Fabry-Perot spectrometer observations of the auroral oval/polar cap boundary above Mawson, Antarctica, *J. Atmos. Terr. Phys.*, *58*(16), 1973–1988, doi:10.1016/0021-9169(96)00007-4.

Innis, J. L., P. Dyson, and P. Greet (1997), Further observations of the thermospheric vertical wind at the auroral oval/polar cap boundary, *J. Atmos. Sol. Terr. Phys.*, *59*(16), 2009–2022, doi:10.1016/S1364-6826(97)00034-5.

Innis, J. L., P. Greet, D. Murphy, M. G. Conde, and P. Dyson (1999), A large vertical wind in the thermosphere at the auroral oval/polar cap boundary seen simultaneously from Mawson and Davis, Antarctica, *J. Atmos. Sol. Terr. Phys.*, *61*(14), 1047–1058, doi:10.1016/S1364-6826(99)00060-7.

Ishii, M., S. Oyama, S. Nozawa, R. Fujii, E. Sagawa, S. Watari, and H. Shinagawa (1999), Dynamics of neutral wind in the polar region observed with two Fabry-Perot interferometers, *Earth Planets Space*, *51*(7–8), 833–844, doi:10.1186/BF03353242.

Ishii, M., M. G. Conde, R. W. Smith, M. Krynicki, E. Sagawa, and S. Watari (2001), Vertical wind observations with two Fabry-Perot interferometers at Poker Flat, Alaska, *J. Geophys. Res.*, *106*(A6), 10,537–10,551, doi:10.1029/2000JA900148.

Larsen, M. F., and J. Meriwether (2012), Vertical winds in the thermosphere, *J. Geophys. Res.*, *117*, A09319, doi:10.1029/2012JA017843.

Makela, J. J., J. Meriwether, J. Lima, E. S. Miller, and S. Armstrong (2009), The remote equatorial nighttime observatory of ionospheric regions project and the international heliospherical year, *Earth Moon Planets*, *104*(1), 211–226.

Makela, J. J., et al. (2014), Storm time response of the midlatitude thermosphere: Observations from a network of Fabry-Perot interferometers, *J. Geophys. Res. Space Physics*, *119*, 6758–6773, doi:10.1002/2014JA019832.

Picone, J. M., A. E. Hedin, D. P. Drob, and A. C. Aikin (2002), NRLMSISE-00 empirical model of the atmosphere: Statistical comparisons and scientific issues, *J. Geophys. Res.*, *107*(A12), 1–16, doi:10.1029/2002JA009430.

Price, G., R. W. Smith, and G. Hernandez (1995), Simultaneous measurements of large vertical winds in the upper and lower thermosphere, *J. Atmos. Terr. Phys.*, *57*(6), 631–643, doi:10.1016/0021-9169(94)00103-U.

Raghavarao, R., W. R. Hoegy, N. W. Spencer, and L. E. Wharton (1993), Neutral temperature anomaly in the equatorial thermosphere—A source of vertical winds, *Geophys. Res. Lett.*, *20*(11), 1023–1026, doi:10.1029/93GL01253.

Rees, D., R. W. Smith, P. Charleton, F. McCormac, N. Lloyd, and A. Steen (1984), The generation of vertical thermospheric winds and gravity waves at auroral latitudes—I. Observations of vertical winds, *Planet. Space Sci.*, *32*(6), 667–684, doi:10.1016/0032-0633(84)90092-8.

Rieger, E. (1974), Neutral air motions deduced from barium releases experiments—I. Vertical winds, *J. Atmos. Terr. Phys.*, *36*(8), 1377–1385, doi:10.1016/0021-9169(74)90214-1.

Ronksley, A. (2016), Optical remote sensing of mesoscale thermospheric dynamics above Svalbard and Kiruna, PhD thesis, Univ. of London.

Sica, R. (1984), Auroral zone thermospheric dynamics using Fabry-Perot interferometric measurements of the OI 15867 K emission, PhD. Thesis, Univ. of Alaska, Fairbanks.

Sipler, D., M. A. Biondi, and M. Zipf (1995), Vertical winds in the midlatitude thermosphere from Fabry-Perot interferometer measurements, *J. Atmos. Terr. Phys.*, *57*(6), 621–629, doi:10.1016/0021-9169(94)00102-T.

Smith, R. W. (1998), Vertical winds: A tutorial, *J. Atmos. Sol. Terr. Phys.*, *60*(14), 1425–1434, doi:10.1016/S1364-6826(98)00058-3.

Smith, R. W., and G. Hernandez (1995), Vertical winds in the thermosphere within the polar cap, *J. Atmos. Terr. Phys.*, *57*(6), 611–620, doi:10.1016/0021-9169(94)00101-S.

Sobolev, V. (1975), *Light Scattering in Planetary Atmospheres*, Pergamon Press, Oxford.

Spencer, N. W., R. F. Theis, L. E. Wharton, and G. R. Carignan (1976), Local vertical motions and kinetic temperature from AE-C as evidence for aurora-induced gravity waves, *Geophys. Res. Lett.*, *3*(6), 313–316, doi:10.1029/GL003i006p00313.

Spencer, N. W., L. E. Wharton, G. R. Carignan, and J. C. Maurer (1982), Thermosphere zonal winds, vertical motions and temperature as measured from Dynamics Explorer, *Geophys. Res. Lett.*, *9*(9), 953–956, doi:10.1029/GL009i009p00953.

Wardill, P., and F. Jacka (1986), Vertical motions in the thermosphere over Mawson, Antarctica, *J. Atmos. Terr. Phys.*, *48*(3), 289–292, doi:10.1016/0021-9169(86)90104-2.

Wescott, E. M., H. Stenbaek-Nielsen, M. G. Conde, M. Larsen, and D. Lummerzheim (2006), The HEX experiment: Determination of the neutral wind field from 120 to 185 km altitude near a stable premidnight auroral arc by triangulating the drift of rocket-deployed chemical trails, *J. Geophys. Res.*, *111*, 1–11, doi:10.1029/2005JA011002.